Catalysis Letters (2024) 154:2852–2865
https://doi.org/10.1007/s10562-023-04514-9

Vanadia Catalysts Supported on Carbon Nitride for Selective Oxidation of Benzyl Alcohol Under Atmospheric Oxygen

Rui-Ming Wang[1] · Meng Feng[1] · Fei Wang[1] · Bing Xue[1] · Jie Xu[1]

Received: 3 September 2023 / Accepted: 2 November 2023 / Published online: 7 December 2023

Abstract

Selective oxidation of benzyl alcohol under atmospheric oxygen is a sustainable route for the synthesis of benzaldehyde. The development of low-cost metal catalysts is a challenging research topic. Herein, supported vanadia catalysts on carbon nitride were prepared using vanadyl acetylacetonate as a precursor through a wet-impregnation method. The synthesized VO/eg-C_3N_4 were characterized by N_2 adsorption–desorption, TG, XRD, FT-IR, XPS, UV–Vis, SEM, and O_2-TPD. The eg-C_3N_4 material could disperse the vanadia species, and the distributions of vanadium cations (V^{5+}/V^{4+}) were largely dependent on the preparation temperature. In the selective oxidation of benzyl alcohol under atmospheric oxygen, the catalysts showed moderate catalytic activity. Under identical reaction conditions, the activity of VO/eg-C_3N_4 was higher than vanadia catalysts supported on SBA-15 and CNTs materials.

Graphical Abstract

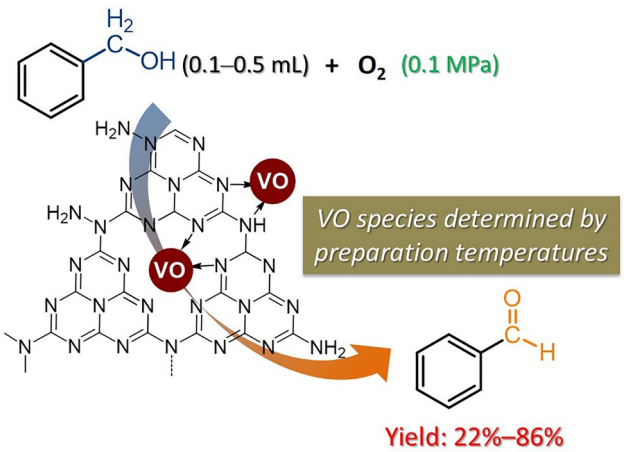

Keywords Vanadium · Graphitic carbon nitride (g-C_3N_4) · Selective oxidation · Benzyl alcohol · Benzaldehyde

1 Introduction

Benzaldehyde (BZL) is the simplest aromatic aldehyde but is widely used in a variety of fields including dyestuff, fragrance, additives, pharmaceuticals, and other fine chemicals [1–3]. Traditionally, BZL was produced by hydrolysis of benzyl chloride derived from toluene chlorination, and the toluene oxidation route [4]. Unfortunately, these two synthetic processes suffer from severe chlorine contamination

✉ Bing Xue
xuebing@cczu.edu.cn

✉ Jie Xu
shine6832@163.com

[1] Jiangsu Key Laboratory of Advanced Catalytic Materials and Technology, School of Petrochemical Engineering, Changzhou University, Gehu Middle Road 21, Changzhou 213164, Jiangsu, People's Republic of China

and metal-containing wastes [5, 6]. Alternatively, liquid-phase selective oxidation of benzyl alcohol (BZA) provides a sustainable approach for the synthesis of BZL. Especially, the oxidation of BZA using molecular oxygen (O_2) as an oxidant has attracted tremendous attention as O_2 is more widely available and economical than other oxidants including hydroperoxide and *tert*-butyl hydroperoxide [2, 7].

Up to now, the most efficient catalysts proposed for the O_2-involved selective oxidation of BZA have been confined to the supported noble metals, such as Pd [8, 9], Pt [10], and Au [11]. Most of these catalysts can be operated under very mild reaction conditions yet demonstrated excellent catalytic conversions of BZA. However, a practical but thorny problem is that such noble catalysts are expensive and rare [12, 13]. Moreover, a basic medium is usually required when they are used in liquid-phase selective oxidation of alcohols [10, 13]. In this sense, exploration of low-cost metal catalysts, especially heterogeneous catalysts, is of interest in green chemistry organic synthesis.

As a conventional metal-oxide catalyst, vanadia has long been applied in numerous catalytic oxidation reactions including oxidation of alkanes [14, 15], alcohols [6, 16], etc. It is commonly believed that the shift of V^{4+} and V^{5+} (redox property) of vanadia based on the Mars−van Krevelen mechanism is responsible for the catalytic activity in O_2-involved reactions [17, 18]. More importantly, the activity of vanadia catalysts is largely related to the catalyst support. To date, the vanadia catalysts supported on silica, alumina, and titania have been intensively studied [15, 16, 19]. It is worth noting that the surfaces of these materials were weakly acidic. On the other hand, alkaline additives were often required in the catalytic selective oxidation of BZA in order to achieve high catalytic activity [10]. Given this fact, the exploration of alkaline catalyst support is more desirable for designing new catalysts for the process.

Graphitic carbon nitride (g-C_3N_4) is a novel carbon-based material and has recently attracted tremendous attention in thermocatalysis and photocatalysis [20–22]. Owing to its abundant nitrogen-containing species in heptazine-based tectonic units, g-C_3N_4 could provide alkaline sites and more importantly facilitate the dispersion of many metal species such as Zn [23], K [24], and Pd [25]. Our group reported oxidation of benzene to phenol catalyzed by vanadia supported on mesoporous carbon nitride (mpg-C_3N_4) [26]. Despite the high catalytic activity, the catalyst support (i.e. mpg-C_3N_4) was prepared by a nanocasting method using silica nanoparticles as sacrificial templates which was very complicated and involved the use of corrosive HF solution. Recently, Wu et al. [27] and Verma et al. [28, 29] reported the preparation of VO/g-C_3N_4 materials and their application of oxidation of ethyl lactate, and hydrocarbons, respectively. However, the catalytic reaction demanded high reaction temperature (130 °C) or light-driven devices. In continuation of our goal to explore effective supported vanadia catalysts for selective oxidation of BZA, herein, exfoliated carbon nitride (eg-C_3N_4) was synthesized by a thermal exfoliation method and then applied as a catalyst support to load vanadia. The eg-C_3N_4 material could disperse the vanadia species, and the distributions of vanadium cations (V^{5+}/V^{4+}) were largely dependent on the preparation temperature. In the selective oxidation of benzyl alcohol under atmospheric oxygen, the VO/eg-C_3N_4 catalysts showed moderate catalytic activity, affording the maximum conversion up to 22.0% at 95 °C.

2 Experimental Section

2.1 Material Preparation

2.1.1 Synthesis of g-C_3N_4 and eg-C_3N_4

Dicyandiamide (5 g, 99%, Aladdin Reagent) was placed into a crucible with a lid and heated from room temperature to 550 °C with a heating slope of 3 °C min^{-1} in a muffle furnace and then tempered at this temperature for another 4 h. The obtained yellow solid was g-C_3N_4.

The exfoliated g-C_3N_4 material was prepared by a thermal exfoliation approach. g-C_3N_4 (2 g) was also placed in a crucible with a lid and heated from room temperature to 600 °C with a heating slope of 3 °C min^{-1}, and tempered for 2 h. The resultant light yellow powder was labeled as eg-C_3N_4.

2.1.2 Preparation of VO/eg-C_3N_4

Vanadyl acetylacetonate ($VO(acac)_2$, $m = 0.15$–0.6 g, 99%, Sinopharm) was dissolved in 20 mL of anhydrous methanol, followed by the addition of 1.6 g of eg-C_3N_4. The mixture was heated under stirring at 50 °C until the removal of methanol. After that, the solid was placed into a crucible and heated from room temperature to a desired temperature ($T = 300$–450 °C, heating slope: 3 °C min^{-1}) and kept at this temperature for another 2 h. The obtained greenish powder was labeled as mVO/eg-C_3N_4-T, where m and T indicated the mass of $VO(acac)_2$ and heating temperature, respectively.

2.1.3 Preparation of VO/eg-C_3N_4-IMP

$VO(acac)_2$ (0.3 g) was dissolved in 20 mL of anhydrous methanol, followed by the addition of 1.6 g of eg-C_3N_4. The mixture was heated under stirring at 50 °C until the removal of methanol. Subsequently, the solid was further heated at 120 °C for another 2 h. The obtained powder was labeled as 0.3VO/eg-C_3N_4-IMP.

2.1.4 Preparation of VO/SBA-15 and VO/CNTs

For comparison, vanadia catalysts were prepared using SBA-15 (mesoporous ordered silica), and carbon nanotubes (CNTs) as supports. The catalyst preparation routes were like that of VO/eg-C_3N_4. The detailed preparation methods of SBA-15 are given in the supporting information.

2.1.5 Preparation of $VO(acac)_2$-400

$VO(acac)_2$ (2 g) was placed into a crucible and heated from room temperature to 400 °C with a heating slope of 3 °C min^{-1}, and kept at this temperature for 2 h.

2.2 Material Characterization

The specific surface areas and porous properties of the materials were analyzed by N_2 adsorption–desorption isotherms at −196 °C using an ASAP 2020 (Micromeritics) instrument. Before the analysis, the samples were pretreated in a vacuum at 150 °C for 6 h. The surface areas were calculated by Brunauer–Emmet–Teller (BET) method.

X-ray diffraction (XRD) patterns were recorded on a D/max 2500 X-ray diffractometer (Rigaku) employing a graphite monochromator (40 kV, 40 mA) equipped with Ni-filtered Cu−*K*α radiation. The detector is a scintillation counter.

The vanadium contents of the VO/eg-C_3N_4 materials were analyzed by Inductively coupled plasma mass spectrometry (ICP-MS) using a NexION 350X spectrometer (PerkinElmer). Before analysis, 0.1 g of each sample was calcinated under 700 °C for 1 h. The obtained powder was added to HCl (2 wt%, a.q.) and heated at 90 °C for 2 h. After that, the clear supernatant was diluted and then analyzed by ICP-MS.

Fourier transform infrared (FT-IR) spectra were tested in a Tensor 27 (Bruker) spectrometer based on the transmission mode with a resolution of 4 cm^{-1} and 32 scans. Before analysis, each sample was mixed with KBr (mass ratio of the sample to KBr was ca. 1:200. KBr: optically pure, Sinopharm) and crushed into thin a pellet (20 MPa of pressure).

UV–Vis diffuse reflectance spectra (DRS) were carried out on a UV-3600 spectrophotometer (Shimadzu) using $BaSO_4$ as a standard reference. The visible and ultraviolet light sources of UV–Vis spectrometer are tungsten halogen and deuterium lamp, respectively.

X-ray photoelectron spectroscopy (XPS) measurements were performed using an ESCALAB 250 XI spectrometer (Thermo Fisher) working in the constant energy mode with Mg K_α radiation as the excitation source. The base pressure of the analytic chamber of ESCALAB 250 XI ca. 2.0×10^{-7} mBar, and the carbonaceous C 1s line (284.6 eV) was used as the reference to calibrate the binding energies. The subsequent data analysis for XPS was performed by means of the XPS Peak 4.1 program. The backgrounds of the V 2p and N 1s spectra were subtracted based on a Shirley function from the region of interest. Afterward, the spectra were fitted according to the binding energies of various bonding-state atoms (components) described in the relevant literature. Wherein, the ratio of Lorentzian−Gaussian function for each fitted peak was kept as 20% of Lorentzian and 80% of Gaussian.

Thermogravimetric (TG) measurements of the catalysts were conducted on a Netzsch TG 209 F3 apparatus. The samples were placed in α-Al_2O_3 crucibles and heated in flowing air (20 mL min^{-1}) from room temperature to 850 °C at a rate of 20 °C min^{-1}.

Scanning electron microscopy (SEM) images were obtained on a Gemini SEM 300 microscope (ZEISS).

Oxygen temperature-programmed desorption (O_2-TPD) was analyzed on a ChemBET-3000 station (Quantachrome). The sample (100 mg, crushed into 20−30 meshes) was pretreated at 200 °C for 1 h under N_2 flow and then cooled down to 50 °C. Next, the sample was heated at 50 °C under He flow (60 mL min^{-1}) for another 30 min. The sample was swept with O_2/He (10 v/v%, 60 mL min^{-1}) for 40 min and He for 30 min. Afterward, the sample was heated from 50 to 550 °C with a ramping rate of 10 °C min^{-1}.

2.3 Catalytic Evaluation

The selective oxidation of BZA was conducted in a three-necked bottomed flask (25 mL) equipped with a condenser and magnetic stirrer. BZA (0.5 mL) and toluene (5 mL) were added to the flask and heated up to 95 °C. Afterward, the catalyst (50 mg) was added to the solution and then purged with oxygen flow (20 mL min^{-1}). The reaction was carried out for 8 h under stirring. During the process, an aliquot (ca. 0.20 mL) of the reaction mixture was collected periodically, centrifuged and the clear supernatant was analyzed by GC. The products in this work only included BZL (target molecule, major product accounting for > 99.9%) and the trace of benzoic acid (BA, < 0.1%); no other products were detected. The carbon balance was determined using *n*-decane as an internal standard and was nearly 100% in this study. The detailed method of carbon balance was given in the support information.

The conversion (*Conv.*) of BZA and selectivity (*Sel.*) to benzaldehyde were calculated by means of an area-normalization method, and the detailed calculation equations were as follows:

$$Conv. = \frac{A_{BZL}\times f_{BZL} + A_{BA}\times f_{BA}}{A_{BZA} + A_{BZL}\times f_{BZL} + A_{BA}\times f_{BA}}$$

$$Sel. = \frac{A_{BZL}\times f_{BZL}}{A_{BZL}\times f_{BZL} + A_{BA}\times f_{BA}}$$

where A and f were the peak area and response factor, respectively, for each component analyzed by GC.

After the completion of the catalytic reaction, the reaction mixture containing the solvent, reactants, products, and the catalyst was filtrated, and the filtered solid was washed with toluene two times (5 min for each time). The final filtrate solid was heated at 80–100 °C overnight. After such a recycling process, only ca. 87% of the catalyst was smoothly recycled.

3 Results and Discussions

3.1 Materials Characterization

Figure 1A shows the N_2 adsorption–desorption isotherms of the g-C_3N_4, eg-C_3N_4, and their supported materials. The g-C_3N_4 material displayed type-IV isothermal curves, along with a minor hysteresis loop between $p/p_0 = 0.85$ to 0.99, suggesting that the materials possessed a certain amount of mesostructured pores. Compared with g-C_3N_4, eg-C_3N_4 had a higher adsorption quantity and the hysteresis loop was evident in the range of 0.75–0.99. This means that eg-C_3N_4 had more mesostructured pores than g-C_3N_4. In the cases of the 0.3VO/eg-C_3N_4-T materials, in spite of less adsorption quantity than the supports, the supported samples also showed type-IV isothermal curves. The corresponding pore sizes of the materials are given in Fig. 1B. These materials had relatively concentrated pore sizes of 2–3 nm, which mainly originated from the interparticle voids. The surface areas and porous information are summarized in Table 1.

The surface area and pore volume of the bare g-C_3N_4 were 17 $m^2\ g^{-1}$ and 0.07 $cm^3\ g^{-1}$, respectively. In comparison, eg-C_3N_4 had larger surface areas and pore volume. The nitrogen-containing species of g-C_3N_4 would decompose themselves during the thermal exfoliation, resulting in more interparticle voids of eg-C_3N_4 [30]. As for the VO/eg-C_3N_4 materials, the surface areas were found to be related to the preparation temperatures.

Figure 2 describes the TG analysis curves of the materials. The eg-C_3N_4 had good thermal stability below 550 °C, while the drastic weight loss occurring from 550 °C was due to the decomposition of the C–N skeleton [31]. By contrast, the pronounced weight loss of $VO(acac)_2$ was acquired at 220–300 °C, corresponding to the decomposition of acetylacetonate functionality. The second weight loss (300–450 °C) was attributed to residual oxygen-containing organic fragments in V_2O_5. The VO/eg-C_3N_4-T materials exhibited different thermal stability. As explained above, eg-C_3N_4 would thermally decompose. In the presence of a metal-containing component such as V in this work, the decomposition would become more severe and occur under lower temperatures. Therefore, for VO/eg-C_3N_4-T composites, adopting higher temperatures can roughly estimate the weight percentage of thermally stable components, as the eg-C_3N_4 component would totally decompose under such conditions. As shown in Fig. 2, the residual weights of 0.3VO/eg-C_3N_4-350/400/450 materials obtained at 600 °C were 27, 61, and 96%, respectively. As the heating temperatures were increased, more parts of eg-C_3N_4 decomposed. As a result, the residual weight percentages of the thermally stable component (probably V_2O_5) were different, and the order

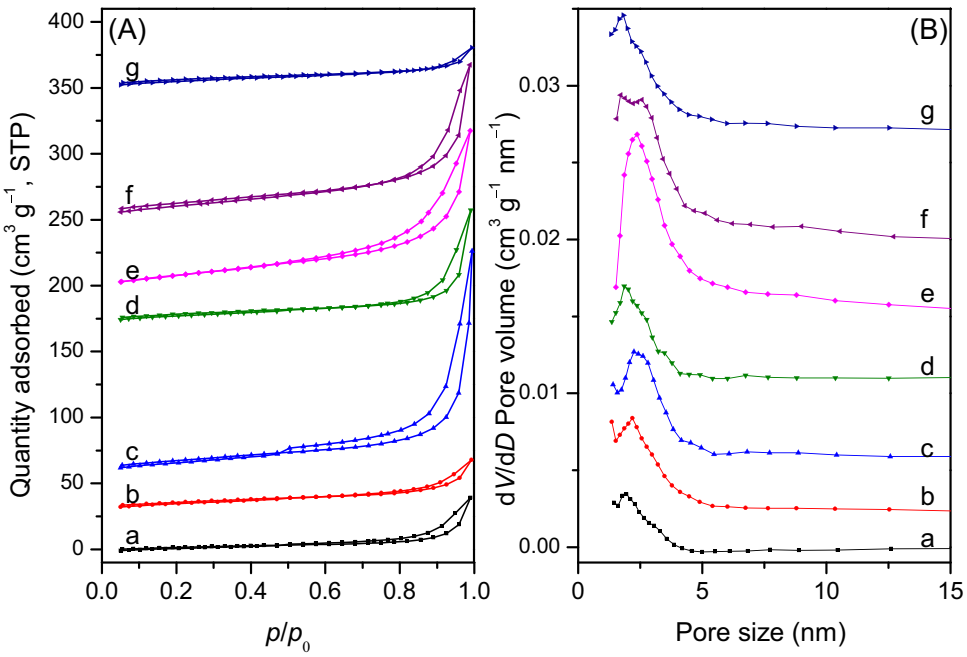

Fig. 1 N_2 adsorption–desorption isotherms (**A**) and corresponding pore size distributions (**B**) of g-C_3N_4 (*a*), 0.3VO/g-C_3N_4-400 (*b*), eg-C_3N_4 (*c*), 0.3VO/eg-C_3N_4-300 (*d*), 0.3VO/eg-C_3N_4-350 (*e*), 0.3VO/eg-C_3N_4-400 (*f*), and 0.3VO/eg-C_3N_4-450 (*g*)

Table 1 Surface areas, pore sizes, and pore volumes of the materials

Material	Surface area ($m^2\ g^{-1}$)	Pore size (nm)	V_p[a] ($cm^3\ g^{-1}$)	V[b] (wt%)	V densities[c] (atom nm^{-2})
g-C_3N_4	17	2.1	0.07	–[d]	–[d]
eg-C_3N_4	49	2.4	0.27	–	–
0.3VO/g-C_3N_4-400	27	2.2	0.06	–	–
0.3VO/eg-C_3N_4-300	29	1.9	0.13	3.0	12.2
0.3VO/eg-C_3N_4-350	61	2.3	0.19	11.1	21.5
0.3VO/eg-C_3N_4-400	63	2.6	0.19	34.1	63.9
0.3VO/eg-C_3N_4-450	25	2.0	0.05	50.5	238.6
0.3VO/CNTs-400	187	2.2	0.39	–	–
0.3VO/SBA-15-400	573	9.4	0.92	–	–

[a]Pore volume

[b]Loading amounts analyzed by ICP-MS

[c]Calculated according to loading amounts (moles of V) and surface areas

[d]Not analyzed

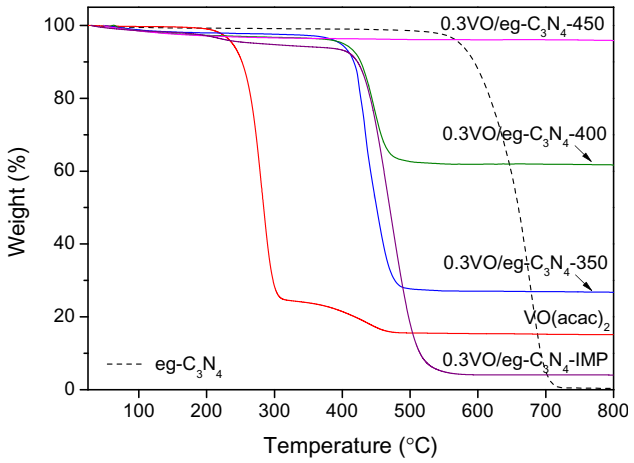

Fig. 2 TG curves of eg-C_3N_4, $VO(acac)_2$, 0.3VO/eg-C_3N_4-*T*, and 0.3VO/eg-C_3N_4-IMP

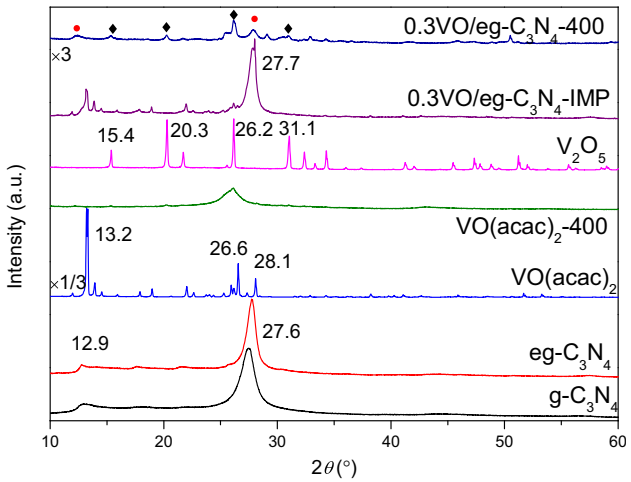

Fig. 3 XRD patterns of g-C_3N_4, eg-C_3N_4, $VO(acac)_2$, $VO(acac)_2$-400, V_2O_5, 0.3VO/eg-C_3N_4-IMP, and 0.3VO/eg-C_3N_4-400. The peaks tagged with ● and ◆ belonged to g-C_3N_4 and V_2O_5 phases

of weight percentages was 0.3VO/eg-C_3N_4-450 > 0.3VO/eg-C_3N_4-400 > 0.3VO/eg-C_3N_4-350. Namely, the ingredient of 0.3VO/eg-C_3N_4-450 was almost entirely V_2O_5, while 0.3VO/eg-C_3N_4-400 had 39 wt% of eg-C_3N_4.

For the 0.3VO/eg-C_3N_4-300 material, because the $VO(acac)_2$ had not completed the major decomposition, the lower surface area and pore volume (Table 1) than those of eg-C_3N_4 might be the partial blockage of eg-C_3N_4 support by the loaded $VO(acac)_2$-related component. As the preparation temperature was raised, the $VO(acac)_2$ precursor underwent drastic decomposition (Fig. 2) and the release of gas inevitably created more pores in eg-C_3N_4 supports. However, extra high preparation temperature would induce the collapse of the eg-C_3N_4 particles, which could explain the low surface area and pore volume obtained in 0.3VO/eg-C_3N_4-450 (Table 1). The V contents of the 0.3VO/eg-C_3N_4 samples were calculated by ICP-MS. As listed in Table 1, the actual loading amounts of V and densities were very high due to the low surface areas of VO/eg-C_3N_4 materials. More importantly, the decomposition of eg-C_3N_4 as found in TG characterization was also a reason for this.

The XRD patterns of the materials are depicted in Fig. 3. Two diffraction peaks were observed at $2\theta = 27.6$ and 12.9° in the pattern of g-C_3N_4, corresponding to the interplanar (i.e. 002) and intraplanar (100) stacking of graphitic structure [30, 32]. The (002) diffraction peak of eg-C_3N_4 showed a slight shift towards a higher 2θ angle (27.7°). This dense packing of graphitic layers of eg-C_3N_4 compared with g-C_3N_4 was attributed to the squeezing of graphitic layers occurring under the thermal exfoliation process [25, 33]. The XRD pattern of $VO(acac)_2$ showed intensive peaks at 13.2, 26.6, and 28.1°, assigned to triclinic structure (JCPDS

23-1965) [34, 35], whereas V_2O_5 possessed orthorhombic structure (JCPDS 72-0433) with four major diffraction peaks at 15.4, 20.3, 26.2, and 31.1°, corresponding to (200), (001), (110), and (310) reflections [35, 36]. These four peaks were also detected in the XRD pattern of 0.3VO/eg-C_3N_4-400 despite its low-intensity diffraction peaks. Besides these peaks, a peak emerging at 27.9° was also found, evidence of graphitic crystalline structure like eg-C_3N_4. Therefore, 0.3VO/eg-C_3N_4-400 consisted of V_2O_5 and g-C_3N_4, in agreement with the above TG results. As for the 0.3VO/eg-C_3N_4-IMP material that was prepared without calcination step, the XRD pattern signified a major peak at 27.7° and other weak peaks at 13.1, 13.8, and 26.2°, pointing out the material was a composite of g-C_3N_4, $VO(acac)_2$, and some probable amorphous components.

XRD patterns of various 0.3VO/eg-C_3N_4-*T* materials were recorded and given in Fig. 4. It is evident that preparation temperature had a significant influence on the crystalline structure. Specifically, for 0.3VO/eg-C_3N_4-300 with a low preparation temperature of 300 °C, graphitic structure ($2\theta = 27.8°$ and 12.9°) were dominant in the XRD pattern. As the temperature was elevated to 350 °C, the intensity of (002) peaks became weak while a shoulder appeared at ca. 25.8°. In the case of 0.3VO/eg-C_3N_4-400, the peaks associated with V_2O_5 were clearly discovered while the peaks of g-C_3N_4 were weakened. By contrast, in the pattern of 0.3VO/eg-C_3N_4-450, there were no diffraction peaks of g-C_3N_4 left and the crystalline structure was solely V_2O_5. This transformation of structure can be explained by the above TG analytic results (Fig. 2). Figure S1 shows the XRD patterns of VO/eg-C_3N_4-400 with various dosages of $VO(acac)_2$ precursor. Like the variation trend in Fig. 4, 0.15VO/eg-C_3N_4-400 was of mainly graphitic structure; as the $VO(acac)_2$ dosage was higher than 0.3 g, the vanadia component prevailed over g-C_3N_4 in VO/eg-C_3N_4-400 materials.

Figure 5 is the FT-IR spectra of the materials including g-C_3N_4, $VO(acac)_2$, V_2O_5, 0.3VO/eg-C_3N_4-400, etc. The g-C_3N_4 and eg-C_3N_4 showed exactly the same spectra. The multiple bands in the range of 1200–1600 cm^{-1} were assigned to the stretching vibration of nitrogen-containing heterocycles, and the sharp bands at 811 cm^{-1} were indexed as the breathing mode of conjugated heptazine units, characteristic of g-C_3N_4 [27, 32]. The broad band at ca. 3200 cm^{-1} was ascribed to the amino (N–H) groups of g-C_3N_4 and adsorbed water molecules (O–H) [27, 37]. As for the spectrum of V_2O_5, the primary band of 1023 cm^{-1} corresponded to isolated V=O vanadyl groups. The bands centered at 834 cm^{-1} and 590 cm^{-1} were assigned to stretching and bending vibration of V–O–V chains, respectively [38, 39]. These three bands were also detected in the spectrum of $VO(acac)_2$-400. This further suggested that $VO(acac)_2$-400 subjected to heating treatment contained vanadia species, which might be amorphous V_2O_5 as revealed in the XRD pattern (Fig. 3). The bands associated with V_2O_5 and g-C_3N_4 were both discovered in the spectrum of 0.3VO/eg-C_3N_4-400. This finding agrees well with the analytic results acquired in XRD patterns (Fig. 3).

For the sake of comparison, we have also prepared supported $VO(acac)_2$ material (0.3VO/eg-C_3N_4-IMP) which was prepared like 0.3VO/eg-C_3N_4-400 but without calcination step. The FT-IR spectrum of 0.3VO/eg-C_3N_4-IMP (Fig. S2) exhibited apparent characteristic bands relevant to g-C_3N_4 while the signals about $VO(acac)_2$ were very weak. Therefore, it is deduced that the calcination procedure indeed resulted in the formation of vanadia component in eg-C_3N_4 support. In addition, the FT-IR spectra of a series of VO/eg-C_3N_4 with various dosages of $VO(acac)_2$

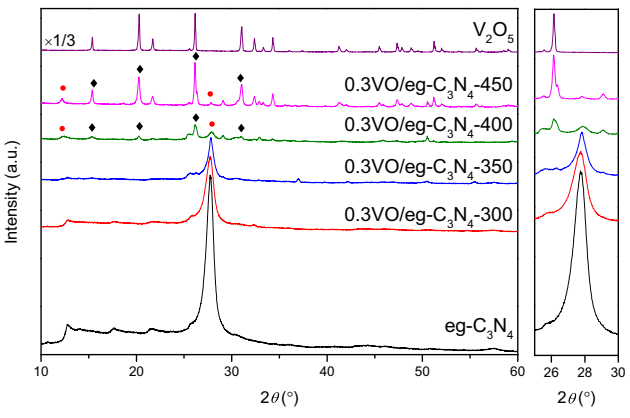

Fig. 4 XRD patterns of eg-C_3N_4, 0.3VO/eg-C_3N_4-300, 0.3VO/eg-C_3N_4-350, 0.3VO/eg-C_3N_4-400, 0.3VO/eg-C_3N_4-450, and V_2O_5. The peaks tagged with ● and ◆ belonged to g-C_3N_4 and V_2O_5 phases

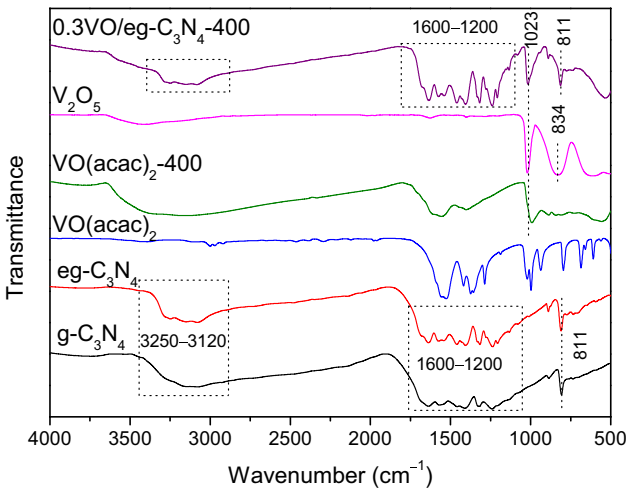

Fig. 5 FT-IR spectra of g-C_3N_4, eg-C_3N_4, $VO(acac)_2$, $VO(acac)_2$-400, V_2O_5, and 0.3VO/eg-C_3N_4-400

and preparation temperatures are depicted in Fig. S3. The 0.3VO/eg-C_3N_4-300 and 0.3VO/eg-C_3N_4-350 were mainly composed by g-C_3N_4 while 0.3VO/eg-C_3N_4-450 was occupied by vanadia. As for *m*VO/eg-C_3N_4-400, it was found that the loading amount of vanadia species had no significance on the ingredient. Namely, these materials were all constituted by vanadia and eg-C_3N_4.

The surface chemical compositions of the materials were analyzed by XPS technique. The spectra (Fig. 6) of V_2O_5 and $VO(acac)_2$ demonstrated signals with binding energies of 531, 523, 516, and 284 eV, corresponding to O 1s, V $2p_{1/2}$, V $2p_{3/2}$, and C 1s orbits. In the case of 0.3VO/eg-C_3N_4-IMP, besides these peaks, a pronounced peak was shown at 398 eV (N 1s). As for 0.3VO/eg-C_3N_4-*T* materials, the peak intensity of N 1s was largely dependent on the preparation temperatures. The spectrum of 0.3VO/eg-C_3N_4-350 resembled that of 0.3VO/eg-C_3N_4-IMP. As the preparation temperature was increased, the peak intensity of N 1s became weaker. Besides N 1s regions, the C 1s regions of 0.3VO/eg-C_3N_4-400 and 0.3VO/eg-C_3N_4-450 materials

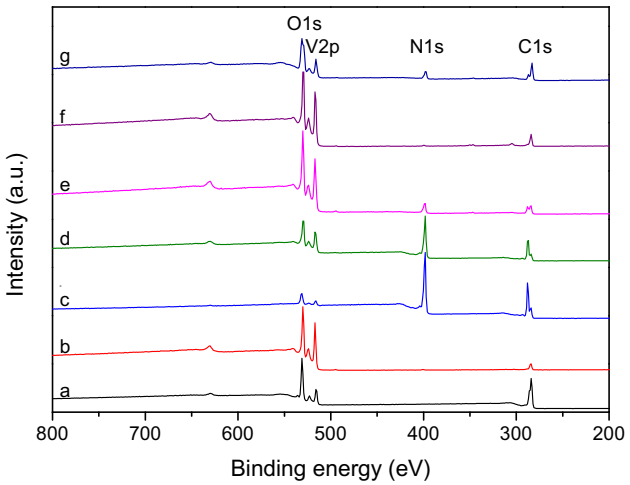

Fig. 6 XPS survey of $VO(acac)_2$ (*a*), V_2O_5 (*b*), 0.3VO/eg-C_3N_4-IMP (*c*), 0.3VO/eg-C_3N_4-350 (*d*), 0.3VO/eg-C_3N_4-400 (*e*), 0.3VO/eg-C_3N_4-450 (*f*), and 0.3VO/eg-C_3N_4-400-R (*g*)

were obviously different from that of 0.3VO/eg-C_3N_4-350. As explained above, the eg-C_3N_4 support underwent partial decomposition during the preparation procedure of 0.3VO/eg-C_3N_4-*T* materials, and the thermal decomposition became more severe under higher temperatures. Therefore, 0.3VO/eg-C_3N_4-350 and 0.3VO/eg-C_3N_4-IMP had similar spectrum regions of C 1s. As for 0.3VO/eg-C_3N_4-400 and 0.3VO/eg-C_3N_4-450, a portion of carbon atoms might not be bonded with nitrogen like the heptazine ring in the eg-C_3N_4, thus the C 1s region demonstrated an apparent change.

According to the integrated peak areas of various elements, the chemical compositions of the materials were calculated, as listed in Table 2. The molar C/N ratio gained in eg-C_3N_4 was 0.797:1, slightly higher than the value (0.75) of ideal g-C_3N_4. This was because of the decomposition of nitrogen-containing species during the exfoliation procedure. The 0.3VO/eg-C_3N_4-IMP samples had a similar C/N ratio with eg-C_3N_4. For the 0.3VO/eg-C_3N_4-*T* materials, the C/N ratios (0.994:1–16.000:1) acquired were considerably higher than the value of 0.3VO/eg-C_3N_4-IMP. The drastic change was also reflected by the above characterization results (Figs. S2, S3) of FT-IR. The V/C ratios are also given in Table 2. Because of the heating treatment where eg-C_3N_4 underwent partial decomposition, the 0.3VO/eg-C_3N_4-350 sample had a higher V/C ratio than 0.3VO/eg-C_3N_4-IMP. In the cases of 0.3VO/eg-C_3N_4-400 and 0.3VO/eg-C_3N_4-450, as the heating temperatures were increased, more parts of eg-C_3N_4 decomposed. As a result, 0.3VO/eg-C_3N_4 has higher V/C ratios but less proportion of eg-C_3N_4, which was in agreement with the above TG analytic results (Fig. 2).

In this work, in order to obtain V_2O_5 component in the catalyst support, the as-made 0.3VO/eg-C_3N_4-IMP sample needed to be calcinated above ca. 400 °C. Meanwhile, the nitrogen species in eg-C_3N_4 support suffered unavoidable partial decomposition.

The high-resolution spectra of V $2p_{3/2}$ of the above materials were recorded and depicted in Fig. 7 (note: as V $2p_{1/2}$ signals were very close to O 1s ones and hence were not adopted for analysis). The V $2p_{3/2}$ spectra of $VO(acac)_2$ and V_2O_5 showed a distinct difference, exhibiting almost single

Table 2 Chemical compositions and molar percentages of various V and N species

Material	C/N[a]	V/C[a]	V^{4+} (%)	V^{5+} (%)	N_a (%)	N_b (%)	N_c (%)
eg-C_3N_4	0.797	–	–	–	72.1	16.3	11.6
$VO(acac)_2$	–	0.215	100	0	–	–	–
V_2O_5	–	–	7.6	92.4	–	–	–
0.3VO/eg-C_3N_4-350	0.994	0.313	17.7	82.3	71.0	20.2	8.8
0.3VO/eg-C_3N_4-400	2.062	1.138	24.2	75.8	65.6	25.4	9.0
0.3VO/eg-C_3N_4-450	16.000	1.324	20.5	79.5	67.6	23.7	8.7
0.3VO/eg-C_3N_4-400-R	3.596	0.519	21.9	78.1	67.1	23.9	9.0
0.3VO/eg-C_3N_4-IMP	0.946	0.136	16.8	83.2	73.7	16.4	9.9

[a]Molar ratios determined by XPS survey

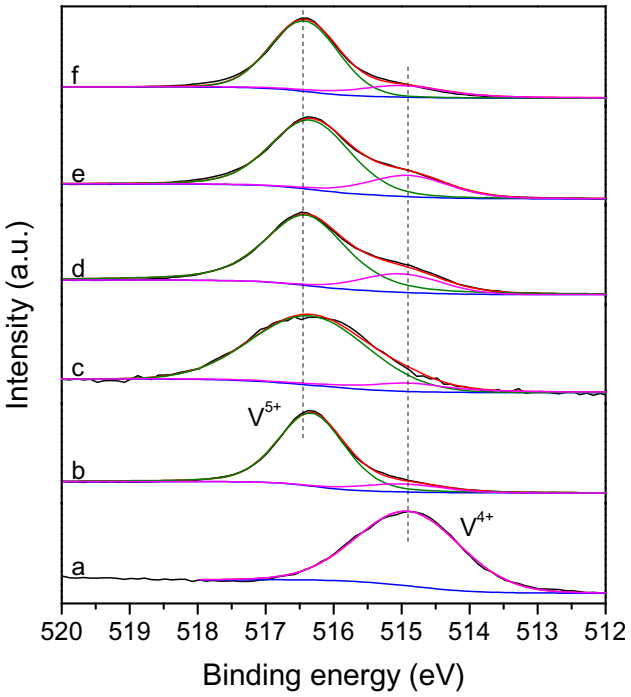

Fig. 7 V $2p_{3/2}$ spectra of $VO(acac)_2$ (*a*), V_2O_5 (*b*), 0.3VO/eg-C_3N_4-IMP (*c*), 0.3VO/eg-C_3N_4-350 (*d*), 0.3VO/eg-C_3N_4-400 (*e*), and 0.3VO/eg-C_3N_4-450 (*f*)

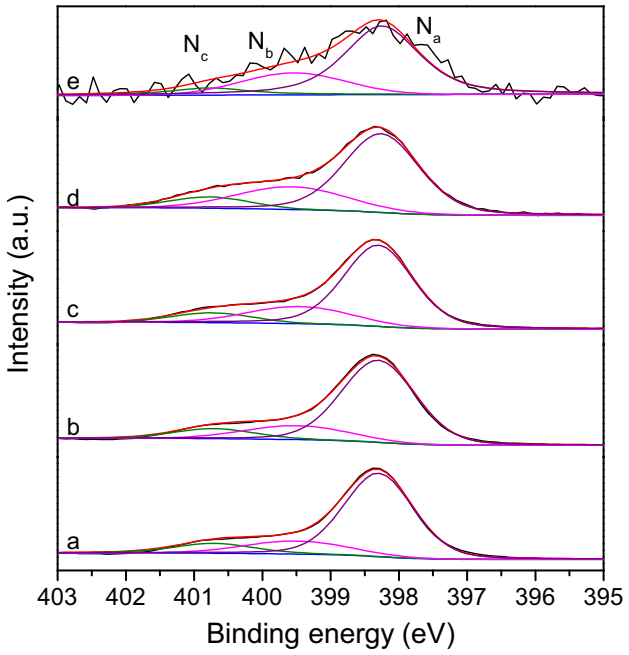

Fig. 8 N 1s spectra of eg-C_3N_4 (*a*), 0.3VO/eg-C_3N_4-IMP (*b*), 0.3VO/eg-C_3N_4-350 (*c*), 0.3VO/eg-C_3N_4-400 (*d*), and 0.3VO/eg-C_3N_4-450 (*e*)

peaks at 515.1 and 516.5 eV that were indexed as V^{4+} and V^{5+} species [17, 40]. By contrast, the spectra of 0.3VO/eg-C_3N_4-IMP and 0.3VO/eg-C_3N_4-*T* could be resolved into two peaks, proving that these materials contained two chemical valences (V^{4+} and V^{5+}). For vanadia-catalyzed oxidative reactions, it is widely recognized that the distributions of vanadium played a crucial role in the final catalytic activity [40]. Considering this point, the detailed fractions of V cations were determined. As listed in Table 2, the percentages of V^{5+} were generally three times higher than that of V^{4+}. Nevertheless, there was still a clear distinction in these materials. Among the three 0.3VO/eg-C_3N_4-*T* materials, 0.3VO/eg-C_3N_4-400 had the highest percentage of V^{4+}. It is of interest to find that 0.3VO/eg-C_3N_4-IMP also owned V^{5+} as much as 83.2%. This might be due to the oxidation of V^{4+} species under ambient conditions. Nevertheless, as signified in XPS (Fig. 6) and FT-IR (Fig. S2) characterization results, the vanadia compound in 0.3VO/eg-C_3N_4-IMP could be partially oxidized $VO(acac)_2$ rather than V_2O_5 like in 0.3VO/eg-C_3N_4-400.

Apart from V $2p_{3/2}$, the high-resolution N 1s spectra were also analyzed. As given in Fig. 8, the spectra of the materials can be deconvoluted into three peaks. The major peaks with the lowest binding energies (398.3 eV) corresponded to sp^2 nitrogen atoms (C=N–C, N_a) bonded in the rings of heptazine, which were dominant in the nitrogen species of eg-C_3N_4. The peaks of 399.1 eV were indexed as nitrogen atoms (N_b) linking adjacent rings of heptazine, and the last peaks with the highest energies (400.7 eV) were ascribed to uncondensed amino groups (N_c) at the edges of g-C_3N_4 sheets. The detailed fractions of various nitrogen species are summarized in Table 2. The VO/eg-C_3N_4 materials had higher fractions of N_b than eg-C_3N_4; this was due to the further condensation of heptazine rings happening during the preparation procedure (calcination) of VO/eg-C_3N_4, which was also reported in the papers involving metal-doped g-C_3N_4 materials [22, 41]. As described above, the nitrogen species of eg-C_3N_4 might anchor metal cations [23, 24]. Here, according to the relevant papers involving vanadia materials supported on carbon nitride [28, 42–44] and the present characterization result of XPS and TG, a possible structure of VO/eg-C_3N_4-400 structure (Scheme 1) was proposed. In VO/eg-C_3N_4-400, vanadia cations included V^{5+} and V^{4+} species, and V^{4+} cations were linked by N_b species of eg-C_3N_4 via coordinate-like interaction.

It was also found that the fractions of N species of VO/eg-C_3N_4 were also related to the preparation temperature. A suitable calcination temperature would facilitate the condensation of adjacent heptazine-based fragments (i.e. transformation of N_a to N_b), while raising the temperature might lead to partial decompositions of N_b species. Among various VO/eg-C_3N_4 samples, 0.3VO/eg-C_3N_4-400 possessed the highest percentage of N_b species, which had superior alkaline strength to N_a and N_c [45, 46]. On the other hand, it is widely realized that an alkaline-medium liquid system is

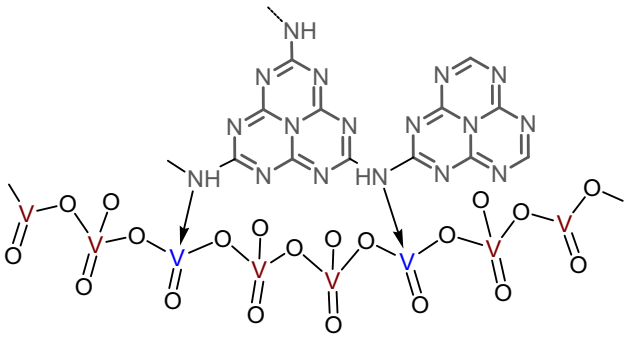

Scheme 1 A possible structure of VO/eg-C_3N_4-400

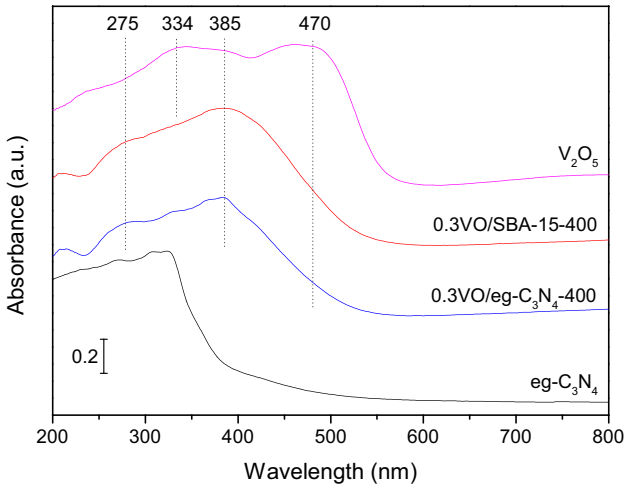

Fig. 9 UV–Vis spectra of eg-C_3N_4, V_2O_5, 0.3VO/eg-C_3N_4-400, and 0.3VO/SBA-15-400 materials

beneficial to the subsequent selective oxidation of alcohols [10, 47, 48]. In this sense, it is anticipated the high percentage of N_b species would favor the catalytic activity of 0.3VO/eg-C_3N_4-400 in the subsequent oxidation of benzyl alcohol.

Figure 9 depicts the UV–Vis spectra of eg-C_3N_4, V_2O_5, 0.3VO/eg-C_3N_4-400, and 0.3VO/SBA-15-400 materials. The spectrum of eg-C_3N_4 revealed pronounced absorption in the UV region, corresponding to the band gap between HOMO and LUMO of conjugated heptazine units of g-C_3N_4 [22, 49], which is a characteristic UV absorption signal of g-C_3N_4. The other three samples signified apparent absorption in the visible region. The remarkable peaks of 334 and 470 nm were found in the spectrum of V_2O_5, indicative of polymerized V=O structures (also called bulk-like V_2O_5 crystallite [50]). By contrast, the spectra of 0.3VO/eg-C_3N_4-400 and 0.3VO/SBA-15-400 demonstrated two peaks at 275 and 385 nm, ascribed to isolated V sites in tetrahedral coordination and polymeric V–O–V species [51, 52], respectively. This means that the supported VO component can also be dispersed on 0.3VO/eg-C_3N_4-400, despite its lower surface area than 0.3VO/SBA-15-400.

SEM was further applied to observe the micro-morphology of the materials. The image of eg-C_3N_4 (Fig. 10) showed dispersed slices with a rough mean size of 200–300 nm. Furthermore, there were also aggregated particles of g-C_3N_4. In the case of 0.3VO/eg-C_3N_4-400, the slices became much smaller. As discussed above, this is due to the further thermal decomposition of eg-C_3N_4 material during the preparation process of VO/eg-C_3N_4. The SEM image of 0.3VO/eg-C_3N_4-450 material revealed agglomerated rods. Figure 11 presents the SEM image and EDX mapping of 0.3VO/eg-C_3N_4-400. It can be found that the carbon, nitrogen, oxygen, and vanadium elements were well dispersed on the material.

For supported vanadia catalysts towards oxygen-involving oxidative reactions, the adsorption and activation of oxygen molecules is a significant factor determining the final catalytic activity. Herein, the O_2-TPD experiments were carried out to analyze the oxygen-activating capability of the materials, and the results are described in Fig. 12. There was a very weak desorption peak (ca. 200–300 °C) in the TPD profile of eg-C_3N_4, which should originate from the physical adsorption of oxygen on its surface. In sharp contrast with V_2O_5 with no clear desorption peak, 0.3VO/eg-C_3N_4-*T*

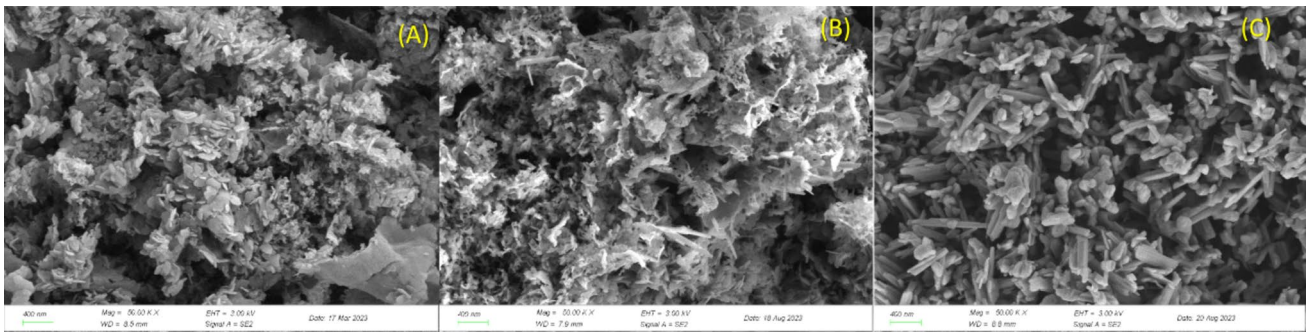

Fig. 10 SEM images of eg-C_3N_4 (**A**), 0.3VO/eg-C_3N_4-400 (**B**), and 0.3VO/eg-C_3N_4-450 (**C**)

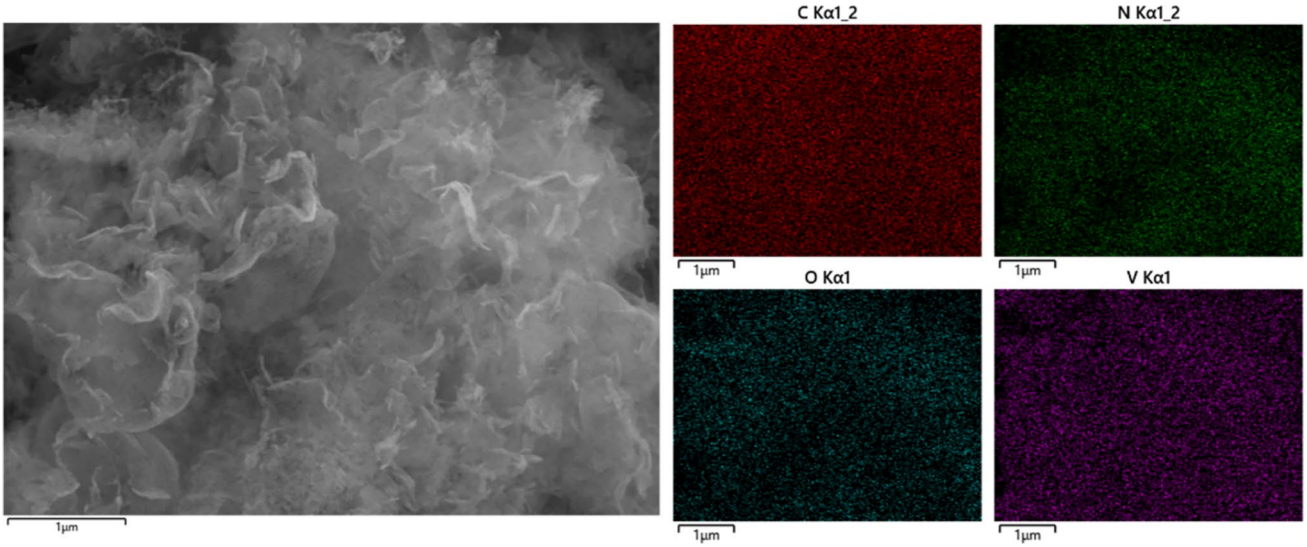

Fig. 11 SEM image and EDX mapping of 0.3VO/eg-C_3N_4-400

materials exhibited evident desorption peaks in the range of ca. 200–400 °C, indicating these materials had relatively strong adsorption ability of oxygen. Furthermore, as illustrated in Fig. 12, 0.3VO/eg-C_3N_4-400 possessed a larger adsorption quantity than the other 0.3VO/eg-C_3N_4-*T* materials. This should be due to its large surface area (Table 1) and higher V^{4+} fractions.

3.2 Catalyst Activity

The selective oxidation reaction of benzyl alcohol by molecular oxygen to benzaldehyde was applied as a target reaction to evaluate the materials. A blank test showed only 1.0% of BZA was converted in the absence of any catalyst (Table 3). In the case of g-C_3N_4 and eg-C_3N_4, the conversions were also very low. The use of $VO(acac)_2$ as a catalyst did not show apparent enhancement in catalytic activity. In addition, the BZA conversions obtained in the cases of $VO(acac)_2$-400 and V_2O_5 were very close (~ 6.0%). As revealed in the XRD patterns (Fig. 3), the composition of $VO(acac)_2$-400 was like amorphous V_2O_5. For the 0.3VO/eg-C_3N_4-300, the catalytic conversion was 3.4%, a little higher than eg-C_3N_4. The catalyst product was almost entirely BZA; a trace of benzoic acid should be due to the subsequent oxidation of BZA. The activity of 0.3VO/eg-C_3N_4-*T* materials was related to the preparation temperature. Among them, 0.3VO/eg-C_3N_4-400 provided the highest BZA conversion, nearly

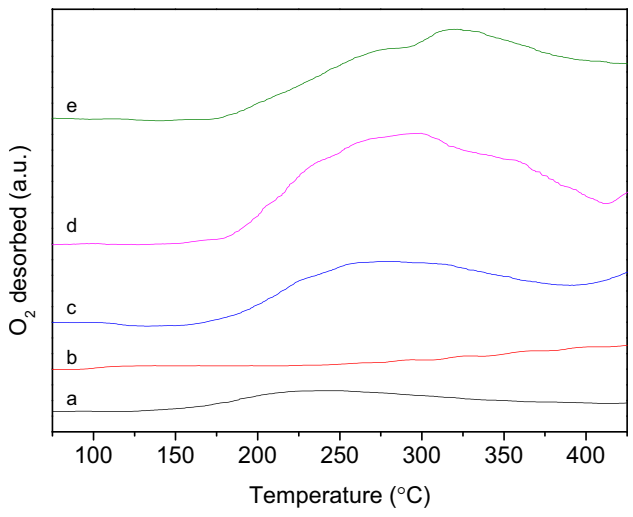

Fig. 12 O_2-TPD profiles of eg-C_3N_4 (*a*), V_2O_5 (*b*), 0.3VO/eg-C_3N_4-350 (*c*), 0.3VO/eg-C_3N_4-400 (*d*), and 0.3VO/eg-C_3N_4-450 (*e*)

Table 3 Catalytic performances of various materials in selective oxidation of BZA

Material	Conv. (%)	Sel. (%)
–	1.0	> 99.9
g-C_3N_4	1.7	> 99.9
eg-C_3N_4	1.9	> 99.9
$VO(acac)_2$	3.7	> 99.9
$VO(acac)_2$-400	5.6	> 99.9
V_2O_5	6.5	> 99.9
0.3VO/eg-C_3N_4-300	3.4	> 99.9
0.3VO/eg-C_3N_4-350	7.8	> 99.9
0.3VO/eg-C_3N_4-400	22.0	> 99.9
0.3VO/eg-C_3N_4-450	13.5	> 99.9
0.3VO/eg-C_3N_4-IMP	7.3	>99.9

Reaction conditions: V_{BZA} = 0.5 mL, 5 mL of toluene, $W_{catal.}$ = 50 mg, T = 95 °C, and t = 8 h

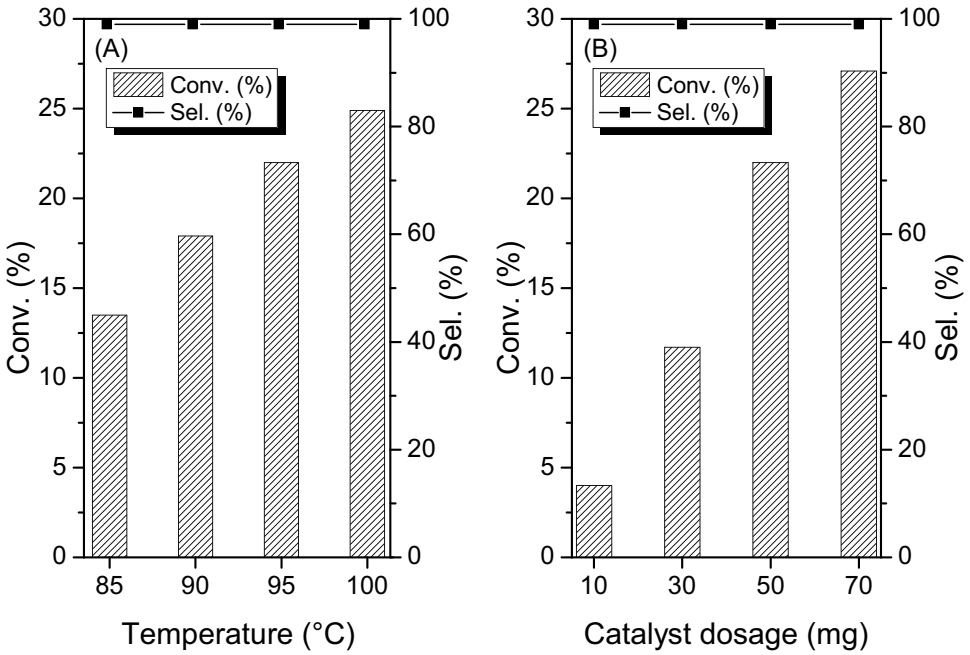

Fig. 13 Influences of reaction temperature (**A**) and catalyst dosage (**B**) on the catalytic results [reaction conditions: V_{BZA} = 0.5 mL, 5 mL of toluene, $W_{catal.}$ = 50 mg (**A**), T = 95 °C (**B**), and t = 8 h]

three times as much as 0.3VO/eg-C_3N_4-350. As described above, the differences between VO/eg-C_3N_4-400 and VO/eg-C_3N_4-350 in terms of surface area (Table 1), V^{4+} fraction, as well as percentage of N_b species (Table 2) were indeed small, whereas the two catalysts exhibited distinct catalytic activities in selective oxidation of benzyl alcohol (Table 3). In this study, the catalytically active sites were considered to be V^{4+} species. However, it is stressed that such V^{4+} species should exist in the form of vanadia coupled with lattice oxygen rather than vanadia-containing complex like $VO(acac)_2$. As revealed in the XRD patterns (Fig. 4), VO/eg-C_3N_4-400 showed obvious diffraction peaks associated with the vanadia compound and g-C_3N_4. By contrast, the pattern of VO/eg-C_3N_4-350 was dominant with diffraction peaks of g-C_3N_4 while the peaks pertaining to vanadia were quite weak. That is, VO/eg-C_3N_4-350 possessed high percentages of V^{4+} and N_b species but limited vanadia species that were indispensable for the catalytic oxidation of benzyl alcohol. As a result, VO/eg-C_3N_4-400 showed remarkably higher catalytic activity than VO/eg-C_3N_4-350. On the other hand, adopting VO/eg-C_3N_4-450 with a higher preparation temperature resulted in a drastic decline in catalytic activity. By comparison, the catalytic performance of the uncalcined sample (0.3VO/eg-C_3N_4-IMP) was evaluated and the resultant BZA conversion was 7.3%.

In the oxidation reaction, the activity of supported vanadia catalysts largely depended on the dispersion of vanadia and the chemical valences of V. Under the same reaction conditions, the catalyst having more fractions of V^{4+} is coupled with more oxygen defects, which are key components to adsorb and activate molecular oxygen. In this sense, 0.3VO/eg-C_3N_4-400 had higher fractions of V^{4+} than its counterparts and more alkaline N_b species, which are responsible for its superior catalytic activity in the selective oxidation of BZA. As for V_2O_5 and 0.3VO/eg-C_3N_4-IMP materials, V_2O_5 has no support and rarely V^{4+} species; although 0.3VO/eg-C_3N_4-IMP possessed appreciable V^{4+} species, the main composition was not vanadia oxide and had not enough oxygen defects.

Table 4 Catalytic performances of various supported VO catalysts in the selective oxidation of BZA

Catalyst	Conv. (%)	Sel. (%)
0.3VO/g-C_3N_4-400	4.9	> 99.9
0.3VO/eg-C_3N_4-400	22.0	> 99.9
0.3VO/CNTs-400	7.5	> 99.9
0.3VO/SBA-15-400	2.5	> 99.9

V_{BZA} = 0.5 mL, 5 mL of toluene, $W_{catal.}$ = 50 mg, T = 95 °C, and t = 8 h

The catalytic performances of various mVO/eg-C_3N_4-400 materials were further investigated. As shown in Table S1, the introduction of the VO component significantly improved the catalytic activity. Nevertheless, as the dosage of $VO(acac)_2$ was greater than 0.3, the resulting catalytic conversion seemed to level off. The evolution of BZA conversion with reaction time is plotted in Fig. S5. The conversion obtained in the first 1 h was only 4.5%. As the reaction was prolonged, the conversion was increased gradually, while after a reaction time of 8 h, no obvious increase was observed.

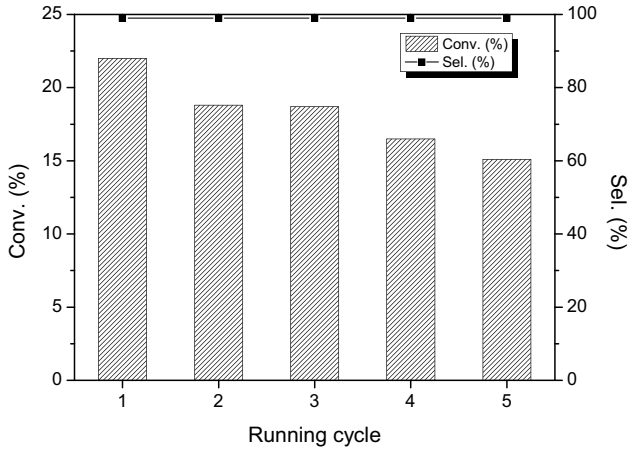

Fig. 14 Catalyst recycling performance of 0.3VO/eg-C_3N_4-400. Reaction conditions: V_{BZA} = 0.5 mL, 5 mL of toluene, $W_{catal.}$ = 50 mg, T = 95 °C, and t = 8 h

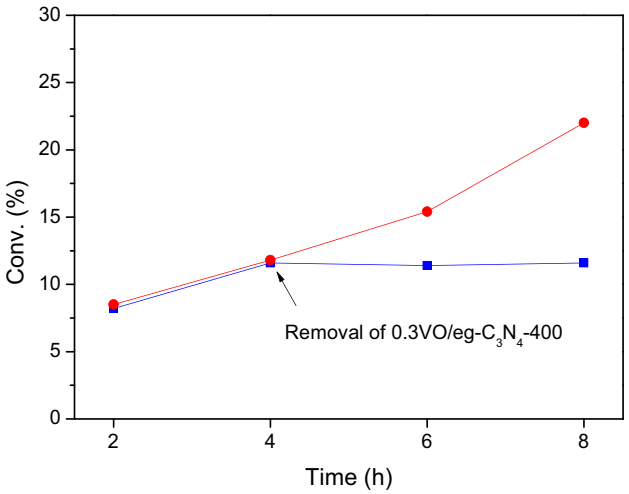

Fig. 15 Hot-filtration catalytic result of 0.3VO/eg-C_3N_4-400

The influences of reaction temperature and catalyst dosage on the catalytic results are depicted in Fig. 13. Under low temperatures, less than 15% of BZA was converted. As the temperature was elevated up to 95 °C, the conversion was drastically increased to 22%. The conversion was also found to be sensitive to the catalyst dosage. Using more catalyst could improve the catalytic conversion. Nonetheless, the increment from 50 to 70 mg was apparently lower than the gap from 30 to 50 mg. Regarding these influences, a reaction temperature of 95 °C and a reaction time of 8 h were chosen as optimal reaction conditions for further investigation. Table S2 shows the catalytic performance of 0.3VO/eg-C_3N_4-400 under various dosages of BZA. With other reaction conditions unchanged, as the feeding dosage of BZA was reduced to 0.1 mL, the conversion of BZA was up to 86.1%.

In many selective oxidation reactions of alcohols catalyzed by metal materials, bases (e.g. K_2CO_3 and KOH) are often required as additives to promote the activation of alcohol substrates [10, 47] and meanwhile restrict the side reaction [53]; however, in this work, we added no alkaline additives into the catalytic reaction. For the sake of comparison, we have prepared vanadia catalysts supported on other materials including CNTs and SBA-15, and evaluated the catalytic activity of the materials. As listed in Table 4, the BZA conversions acquired in the case of 0.3VO/SBA-15-400 and 0.3VO/CNTs-400 were 2.5 and 7.5%, though the two materials had larger surface areas than 0.3VO/eg-C_3N_4-400 (Table 1; Fig. S4). The differences in catalytic activity should be derived from the basicity of the catalyst supports. The eg-C_3N_4 is inherently a solid base which would be more beneficial in activating BZA molecule than the base-free SBA-15 and CNTs.

To examine the recyclability of the 0.3VO/eg-C_3N_4-400 catalyst, recycling experiments were carried out. After each catalytic run, the catalyst was filtrated and used again without any further treatment. During the five consecutive runs, the selectivities were all nearly 100% (Fig. 14). The BZA conversion decreased gradually from 22 to 15%, and the decline in conversion was largely due to the partial loss of catalyst during the recycling procedure. The characterization of FT-IR (Fig. S2) showed that there were no apparent changes in chemical functionalities between the fresh and recycled 0.3VO/eg-C_3N_4-400 catalyst. Furthermore, the V 2p (Fig. S6) and N 1s (Fig. S7) spectra and the corresponding fractions (Table 2) of various V and N species acquired in the recycled 0.3VO/eg-C_3N_4-400 catalyst were also close to those obtained in the fresh one, further suggesting there chemical compositions of 0.3VO/eg-C_3N_4-400 were relatively stable in the selective oxidation of reaction.

Besides the recycling test, we conducted a hot-filtration experiment. As the reaction proceeded for 4 h, the reaction mixture was filtrated immediately. The catalyst was separated and the remaining liquid phase continued to react in the absence of catalyst. As described in Fig. 15, in sharp contrast to the normal process of catalytic reaction, the conversions gained in the hot-filtration experiment showed no further increase, indicating that the active sites of catalysts had not leached out into the reaction system.

4 Conclusion

In summary, VO/eg-C_3N_4 materials were prepared using $VO(acac)_2$ as a precursor and eg-C_3N_4 as a catalyst support. The preparation temperatures played a crucial role in determining the components of materials, as well as the fractions of V cations and nitrogen species. In the selective oxidation of benzyl alcohol using oxygen as an oxidant, VO/eg-C_3N_4 showed moderate catalytic activity, affording the moderate conversion up to 22.0% at 95 °C, much higher than vanadia catalysts supported on SBA-15 and CNTs. This was attributed to nitrogen species of eg-C_3N_4 as alkaline sites that could promote the reaction. Moreover, the catalysts had relatively stable recycling performance.

Supplementary Information The online version contains supplementary material available at https://doi.org/10.1007/s10562-023-04514-9.

Acknowledgements This work was supported by the National Natural Science Foundation of China (22278041), the foundation of CNPC-CZU Innovation Alliance (CCIA2023-02), and the Advanced Catalysis and Green Manufacturing Collaborative Innovation Center. J. Xu also thanks the Shiyanjia Lab (www.shiyanjia.com) for the help in XPS characterization.

Declarations

Conflict of interest There are no conflict of interest to declare for each contributing author.

References

1. Bao X, Li H, Wang Z, Tong F, Liu M, Zheng Z, Wang P, Cheng H, Liu Y, Dai Y, Fan Y, Li Z, Huang B (2021) Appl Catal B 286:119885
2. Xiao Y, Liang L, Liu Z, Yin X, Yang X, Ding Y, Du Z (2022) Appl Surf Sci 585:152668
3. Gueci L, Ferrante F, Prestianni A, Di Chio R, Patti AF, Duca D, Arena F (2020) Inorg Chim Acta 511:119812
4. Della Pina C, Falletta E, Rossi M (2008) J Catal 260:384–386
5. Valentini F, Ferracci G, Galloni P, Pomarico G, Conte V, Sabuzi F (2021) Catalysts 11:262
6. Yi X-T, Wang T-L, Wen L-Z, Xu J, Xue B (2022) Catal Lett 152:962–971
7. Song H, Liu Z, Gai H, Wang Y, Qiao L, Zhong C, Yin X, Xiao M (2019) Front Chem 7:458
8. Wang Z, Zhang B, Yang S, Yang X, Meng F, Zhai L, Li Z, Zhao S, Zhang G, Qin Y (2022) J Catal 414:385–393
9. Zhang L, Chen R, Tu Y, Gong X, Cao X, Xu Q, Li Y, Ye B, Ye Y, Zhu J (2023) ACS Catal 13:2202–2213
10. Gu Q, Sautet P, Michel C (2018) ACS Catal 8:11716–11721
11. Zhang W, Xiao Z, Wang J, Fu W, Tan R, Yin D (2019) ChemCatChem 11:1779–1788
12. Zou H, Xiao G, Chen K, Peng X (2018) Dalton Trans 47:13565–13572
13. Zhu J, Faria JL, Figueiredo JL, Thomas A (2011) Chemistry 17:7112–7117
14. Schumacher L, Weyel J, Hess C (2022) J Am Chem Soc 144:14874–14887
15. Schumacher L, Hess C (2021) J Catal 398:29–43
16. Koivikko N, Ojala S, Laitinen T, Lopes da Silva F, Hautala L, El Assal Z, Honkanen M, Vippola M, Huuhtanen M, Huttula M, Maunula T, Keiski RL (2022) Appl Catal B 318:121803
17. Zavahir S, Xiao Q, Sarina S, Zhao J, Bottle S, Wellard M, Jia J, Jing L, Huang Y, Blinco JP, Wu H, Zhu H-Y (2016) ACS Catal 6:3580–3588
18. Langeslay RR, Kaphan DM, Marshall CL, Stair PC, Sattelberger AP, Delferro M (2019) Chem Rev 119:2128–2191
19. Huang Z, Yan F, Yuan G (2017) Catal Lett 147:509–516
20. Ruban SM, Ramadass K, Singh G, Talapaneni SN, Kamalakar G, Gadipelly CR, Mannepalli LK, Sugi Y, Vinu A (2023) Sci Technol Adv Mater 24:2188879
21. Kong L, Wang J, Ma F, Sun M, Quan J (2019) Appl Mater Today 16:388–424
22. Qureshi WA, Haider SN-U-Z, Naveed A, Ali A, Liu Q, Yang J (2023) Int J Hydrog Energy 48:19459–19485
23. Zhang D, Xu T, Li C, Xu W, Wang J, Bai J (2019) J CO2 Util 34:716–724
24. Bahuguna A, Kumar A, Chhabra T, Kumar A, Krishnan V (2018) ACS Appl Nano Mater 1:6711–6723
25. Yi X-T, Zhao T, Wang F, Xu J, Xue B (2021) New J Chem 45:13519–13528
26. Xu J, Jiang Q, Chen T, Wu F, Li Y-X (2015) Catal Sci Technol 5:1504–1513
27. Wu J, Hua W, Yue Y, Gao Z (2020) ACS Omega 5:16200–16207
28. Verma S, Baig RBN, Nadagouda MN, Varma RS (2016) ACS Sustain Chem Eng 4:2333–2336
29. Verma S, Baig RBN, Nadagouda MN, Varma RS (2016) ACS Sustain Chem Eng 4:1094–1098
30. Ahmad KN, Wan Isahak WNR, Rosli MI, Yusop MR, Kassim MB, Yarmo MA (2022) Appl Surf Sci 571:151321
31. Zhu J, Xiao P, Li H, Carabineiro SAC (2014) ACS Appl Mater Inter 6:16449–16465
32. Bojdys MJ, Müller J-O, Antonietti M, Thomas A (2008) Chemistry 14:8177–8182
33. Li Y, Xu H, Ouyang S, Lu D, Wang X, Wang D, Ye J (2016) J Mater Chem A 4:2943–2950
34. Wang X, Wang S, Zhang Y, Du H (2018) J Mater Sci 53:9701–9709
35. Su DW, Dou SX, Wang GX (2014) J Mater Chem A 2:11185–11194
36. Das B, Sharma M, Baruah MJ, Mounash BP, Karunakar GV, Bania KK (2020) J Environ Chem Eng 8:104268
37. Su Q, Sun J, Wang J, Yang Z, Cheng W, Zhang S (2014) Catal Sci Technol 4:1556–1562
38. Tong D-S, Yao J, Wang Y, Niu H-Y, Wang G-Y (2007) J Mol Catal A 268:120–126
39. Kristensen SB, Kunov-Kruse AJ, Riisager A, Rasmussen SB, Fehrmann R (2011) J Catal 284:60–67
40. Wu Y, Kong L-H, Ge W-T, Zhang W-J, Dong Z-Y, Guo X-J, Yan X, Chen Y, Lang W-Z (2022) J Catal 413:668–680
41. Zhu Y, Zhang X-W, Wang F, Xue B, Xu J (2023) Catalysts 13:828
42. Xu J, Wu F, Jiang Q, Li Y-X (2015) Catal Sci Technol 5:447–454
43. Xu J, Chen Y, Hong Y, Zheng H, Ma D, Xue B, Li Y-X (2018) Appl Catal A 549:31–39
44. Ding G, Wang W, Jiang T, Han B, Fan H, Yang G (2013) ChemCatChem 5:192–200
45. Su F, Antonietti M, Wang X (2012) Catal Sci Technol 2:1005–1009
46. Xu J, Gan Y-L, Pei J-J, Xue B (2020) Mol Catal 491:110979
47. Li Y, Chatterjee A, Chen LB, Lam FL-Y, Hu X (2020) Mol Catal 488:110869
48. da Silva JM, Sousa RC, Costa JCS, Magalhães JL, Luz GE, de Moura CVR, de Moura EM (2022) Catal Lett 152:585–599
49. Wen J, Xie J, Chen X, Li X (2017) Appl Surf Sci 391:72–123
50. Liu Y-M, Cao Y, Yi N, Feng W-L, Dai W-L, Yan S-R, He H-Y, Fan K-N (2004) J Catal 224:417–428

51. Baltes M, Cassiers K, Van Der Voort P, Weckhuysen BM, Schoonheydt RA, Vansant EF (2001) J Catal 197:160–171
52. Berndt H, Martin A, Brückner A, Schreier E, Müller D, Kosslick H, Wolf GU, Lücke B (2000) J Catal 191:384–400
53. Velusamy S, Punniyamurthy T (2004) Org Lett 6:217–219